Geophysical Journal International

Geophys. J. Int. (2025) **244,** 1–13
Advance Access publication 2025 October 17
Research Paper

https://doi.org/10.1093/gji/ggaf416

Reflection seismic profiling of mantle structure under the contiguous United States from ambient noise cross-correlation

Peter M. Shearer [1], Wenyuan Fan [1], S. Shawn Wei [2] and Catherine A. Rychert [3]

[1] *Scripps Institution of Oceanography, UC San Diego, La Jolla, CA* 92037, *USA. E-mail: pshearer@ucsd.edu*
[2] *Department of Earth and Environmental Sciences, Michigan State University, East Lansing, MI* 48824, *USA*
[3] *Woods Hole Oceanographic Institution, Falmouth, MA* 02543, *USA*

Accepted 2025 October 15. Received 2025 October 9; in original form 2025 August 18

SUMMARY

P-wave reflections from the 410- and 660-km mantle discontinuities are visible in stacks of ambient noise cross-correlation functions of USArray stations spanning the contiguous United States. The reflections are most visible on the vertical components at frequencies between 0.1 and 0.3 Hz during low-noise periods, which generally occur during the summer months in the Northern Hemisphere. Common reflection point stacking can be used to resolve apparent lateral differences in discontinuity structure across the continent and suggests the possible existence of sporadic reflectors at other depths. Visibility of the 660-km reflector is correlated with faster *P*-wave velocities at similar depth in a tomographic model for North America. However, the lack of clear agreement between these *P*-wave ambient noise features and prior mantle-transition-zone imaging studies using other methods suggests caution should be applied in their interpretation. Ambient noise sources from the southern oceans may not be distributed uniformly enough for cross-correlation stacks to provide unbiased estimates of the true station-to-station *P*-wave Green's functions. However, the clear presence of 410- and 660-km reflections in the ambient noise data suggests that it should be possible to unravel the complexities associated with varying noise source locations to produce reliable *P*-wave reflection profiles, providing new insights into mantle structure under the contiguous United States.

Key words: Body waves; Seismic discontinuities; Seismic noise.

1 INTRODUCTION

The USArray seismic experiment, which spanned the contiguous United States from 2005 to 2016 with a nominal station spacing of about 70 km, has provided a wealth of new information about mantle structure and the tectonic history of North America. Seismic studies of USArray data have resolved 3-D velocity variations by applying teleseismic body-wave tomography (e.g. Obrebski *et al.* 2010; Schmandt & Humphreys 2010; Sigloch 2011; Burdick & Lekić 2017; Burdick *et al.* 2017; Boyce *et al.* 2023), surface-wave tomography (e.g. Yang & Ritzwoller 2008b; Yang *et al.* 2011; Babikoff & Dalton 2019) and joint body- and surface-wave tomography (e.g. Obrebski *et al.* 2011; Porritt *et al.* 2014; Schmandt & Lin 2014; Golos *et al.* 2018). In addition, upper-mantle discontinuity structure has been examined using *P* receiver functions (e.g. Cao & Levander 2010; Gao & Liu 2014; Schmandt *et al.* 2014; Burky *et al.* 2023; Carr *et al.* 2025; Luo *et al.* 2025), *S* receiver functions (e.g. Kind *et al.* 2015; Hopper & Fischer 2018; Bissig *et al.* 2021) and topside *SH*-wave reflections (e.g. Shearer & Buehler 2019; Liu & Shearer 2021).

Cross-correlation of ambient seismic noise (e.g. Campillo & Paul 2003; Paul *et al.* 2005; Yang & Ritzwoller 2008a) is now widely used to resolve surface waves and ambient noise analyses have been applied in USArray surface-wave tomography studies (e.g. Bensen *et al.* 2008; Lin *et al.* 2008, 2009). Ambient noise methods can also be applied to extract core and mantle body waves (e.g. Poli *et al.* 2012a, b; Boué *et al.* 2013; Lin *et al.* 2013; Nishida 2013), but this has generally proven more challenging than surface-wave ambient-noise analyses because of weaker body-wave amplitudes. Several studies have shown that near-vertical *P*-wave reflections from the 410- and 660-km mantle discontinuities are visible in cross-correlation analyses of station pairs separated by distances of up to a few hundred kilometres (e.g. Poli *et al.* 2012a; Feng *et al.* 2017; Li *et al.* 2019; Feng *et al.* 2021, 2022; Pedersen *et al.* 2023; Chen *et al.* 2025; Zhang *et al.* 2025; Aiman *et al.* 2025b).

Building on these results, here we apply ambient noise cross-correlation to about 1700 seismic stations from the USArray experiment to extract body-wave phases. We find that top-side upper-mantle discontinuity reflections from the 410- and 660-km discontinuities are visible at short periods (3 to 10 s) during low-noise peri-

ods, which generally occur during summer months in the Northern Hemisphere. Common-reflection point (CRP) stacking of the cross-correlation functions reveals substantial apparent lateral variability in the 410- and 660-km reflectors as well as possible evidence for reflectors at other depths. We evaluate whether these features can be taken at face value or whether further work is needed to improve their reliability, given the spatial and temporal variability of oceanic noise sources.

2 DATA PROCESSING

We use 2005 to 2016 continuous seismograms from USArray, a transportable network of over 400 broad-band seismic stations that moved across the contiguous United States for over 10 yr (Meltzer *et al.* 1999; Iris 2003). To reduce computation and memory requirements, we only analyse velocity waveforms stored at 1 sample-per-second. Following previous work, we focus on the secondary microseism band and filter the data to between 0.1 and 0.3 Hz (3 to 10 s period). We then compute and save measures of the average daily vertical amplitudes and horizontal-to-vertical (H/V) ratios within this band as follows:

(i) In each hour, we separately average the squares of the vertical component and the two horizontal components.
(ii) We compute an hourly amplitude measure as $\log_{10}$ of the square root of the vertical average.
(iii) We compute an hourly H/V ratio measure as the square root of the ratio of the sum of the two horizontal components to the vertical component sum.
(iv) We compute daily amplitude and H/V measures by averaging the hourly measures.

When computing cross-correlations, we do not attempt to remove earthquake signals, but we reduce their effect by compressing the waveform amplitudes using a time-domain filter that normalizes each point with a centred 15-point running average of the absolute values of the 0.1–0.3 Hz filtered data. Next we compute daily single-station autocorrelation functions and cross-correlation functions from the filtered data for every pair of stations separated by 250 km or less, allowing time-shifts of up to ±250 s. To save space, we average the positive and negative parts of the cross-correlation functions. For the entire USArray data set, this produces over 13 million cross-correlation functions, which we save as one binary file per day for subsequent processing.

Some previous work has shown that discontinuity phases are seen more clearly when phase-weighted stacking (PWS) (Schimmel & Paulssen 1997) is applied to the cross-correlation functions (e.g. Feng *et al.* 2017; Li *et al.* 2019). We did not experiment with PWS but found that an nth-root stack (Kanasewich *et al.* 1973) produces improved results compared to simple linear stacking of the cross-correlation functions. For all the results presented here we use $n = 5$, which greatly compresses the amplitudes but is not as extreme as a sign-bit filter.

Pedersen *et al.* (2023) found that top-side P-wave reflections from the 410- and 660-km discontinuities ($P410P$ and $P660P$, following the naming convention that PdP denotes a single topside P-wave reflection at depth d between a surface source and receiver) under the Alps region of Europe could be seen more clearly in noise correlation results during periods of low H/V ratios. Because temporal variations in H/V across Europe are caused by the relative strength of surface waves (mostly generated in the North Atlantic and eastern Mediterranean Sea) to near-vertically travelling P waves from sources in the Southern Hemisphere (Lu *et al.* 2022), the H/V ratio can be used to identify times of lower contamination by surface waves and thus more favourable conditions for observing body-wave signals from the deep Earth. In Europe, these favourable times with low H/V ratios occur most often during June–August, when wave-generating storms are less intense in the Northern Hemisphere (producing weaker surface waves) and more intense in the Southern Hemisphere (producing stronger body waves) (Lu *et al.* 2022; Pedersen *et al.* 2023).

Across the United States, we also find that $P410P$ and $P660P$ are more visible during the Northern Hemisphere summer but that the average amplitude on the vertical component is a better predictor of reflector visibility than the average H/V ratio. This is illustrated in Fig. 1, which shows stacks for daily cross-correlation functions for all USArray stations between 35° and 40° latitude during 2012 and most of 2013. Fig. 1(a) shows stacks binned at 20-km intervals in station separation distance and plotted versus distance. The near-vertical lines (red) at about 100 and 150 s show predicted arrival times for $P410P$ and $P660P$ based on the iasp91 velocity model (Kennett & Engdahl 1991). The diagonal line (blue) shows the approximate ending time of the surface-wave arrivals in the cross-correlation functions, which we use to exclude the surface-wave-contaminated times from stacking. Note that the 'noise' in the stacks at times beyond the expected $P660P$ arrival decreases with the number of traces stacked (the *fold* in the language of reflection seismology). For example, the stack at 40 to 60 km separation distance sums only 15 671 cross-correlation functions and appears much noisier than the stack at 60 to 80 km separation distance, which sums 106 623 traces. The absence of station separation distances less than about 50 km is caused by the target USArray station spacing of about 70 km; the results shown at zero distance are from autocorrelation functions.

To combine results from different station separation distances, we convert each cross-correlation function from time to depth. We generate a depth profile sampled at 5-km depth intervals up to 1000 km by using the iasp91 velocity model to predict the traveltime for a reflector at each depth increment. This time will not exactly align with our 1-s data sample rate, so we suitably interpolate the values in the cross-correlation functions to generate the values for the depth profiles. We exclude from the depth profiles any depths that correspond to times earlier than the surface-wave limit (the diagonal (blue) curve in the figure). Fig. 1(b) shows the result of stacking and averaging the depth profiles derived from the 1178 574 total cross-correlation functions in this example. Note that $P660P$ is visible but $P410P$ is at or below the noise level.

Fig. 1(c) shows the depth profile stacks as a function of time (days from 2012 January 1). Here both $P410P$ and $P660P$ are visible as vertical streaks but only during limited time periods. For comparison, the right two panels show the average daily log vertical-component amplitude and H/V measures. The amplitude measure shows clear seasonal variations that inversely correlate with $P410P$ and $P660P$ visibility. That is, the discontinuity reflectors are most visible during low-amplitude periods, which are mostly in the Northern Hemisphere summer months (May to August). In contrast, the H/V measure shows much more limited seasonal variations.

Motivated by this result, we apply an amplitude cutoff and stack the cross-correlation functions (and depth-converted profiles) only for the 209 d with average vertical amplitude measures less than or equal to 2.9. These results are shown in Fig. 2. Although far fewer total cross-correlation functions are stacked (357 514 versus

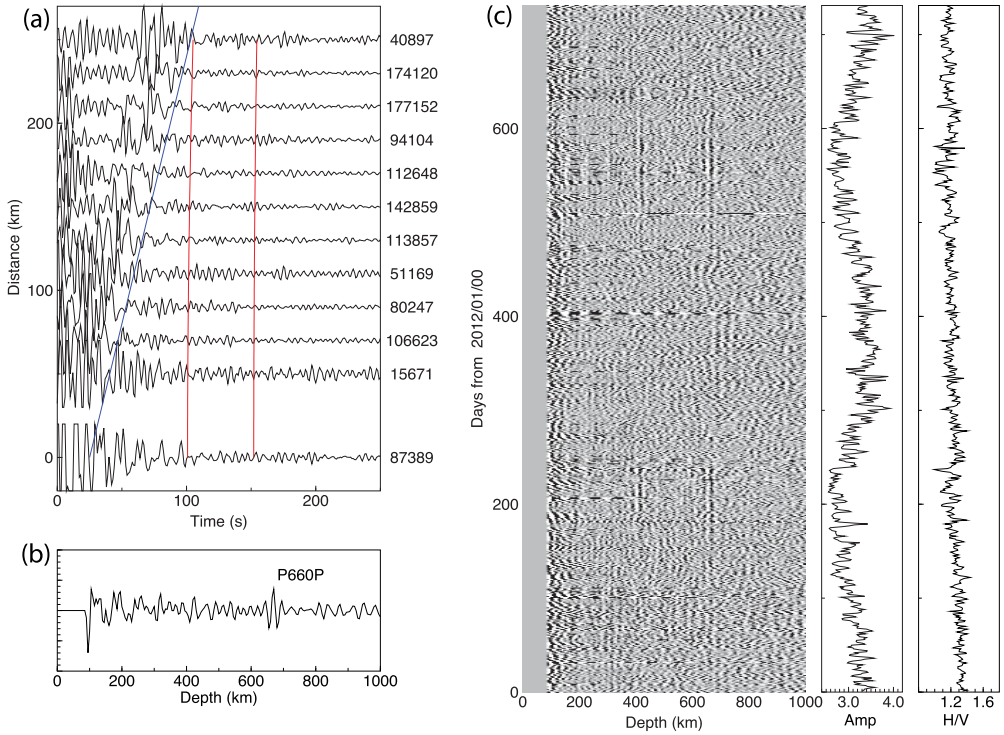

Figure 1. (a) Stacks of USArray ambient noise cross-correlation functions, binned at 20 km intervals in station separation distance. The number of daily cross-correlation functions contributing to each stack is labelled on the right. The near-vertical lines (red) at about 100 and 150 s show predicted arrival times for the topside $P410P$ and $P660P$ reflections. The diagonal line (blue) defines the approximate extent of the surface wave energy and is used to limit contributions to the depth profile stacks. (b) A sum of the cross-correlation functions after conversion from time to depth based on the iasp91 velocity model (Kennett & Engdahl 1991). The $P660P$ reflection is labelled. (c) Daily depth profile stacks shown as a function of days since 2012 January 1. Positive values are black and negative values are white. For plotting purposes, the stack values are increased with depth, z, as $(z-100)^{1.2}$ to compensate for generally decreasing amplitudes at deeper depths. The right panels show a measure of the average daily amplitude and H/V ratio (see the text for details). Note that the 410- and 660-km reflections appear as the vertical streaks in the image during low-amplitude periods, which mainly occur during the Northern Hemisphere summer.

1178 574), both $P410P$ and $P660P$ are visible with greater clarity in Fig. 2(b) compared to the previous figure. This is consistent with the results of Pedersen *et al.* (2023) for the Alps region of Europe, who found that stacking a subset of the data during times of low H/V ratios (e.g. June through August) improved the signal-to-noise of $P410P$ and $P660P$ compared to stacking the complete data set. However, we find for the USArray data that a measure of average vertical-component amplitude works better than the H/V ratio to define the favourable stacking periods.

To include more station pairs and extend our depth coverage, we repeated the waveform cross-correlation calculation for our entire USArray data set only for the days with average vertical amplitude measures less than or equal to 2.9, while increasing the maximum station separation distance from 250 to 300 km and the cross-correlation time-shifts from ± 250 to ± 300 s. This resulted in about 12 million total cross-correlation functions from the low surface-wave noise periods, which form the basis of the analyses that follow.

To image lateral variations in upper-mantle reflectors, we first convert every autocorrelation and cross-correlation function to a depth profile extending to 1200 km using the iasp91 velocity model, assuming the ray path for the station-to-station Green's function, that is, a Snell's law reflection at the bouncepoint. To avoid surface-wave contamination, we exclude cross-correlation times less than $20 + x/2.7$, where x is station separation distance (km) and 2.7 is velocity in km s^{-1}. We then consider a grid of reflector locations, spaced at 1-degree intervals in both latitude and longitude. At each grid point, we then search for station-pair midpoints (or autocorrelation station locations) within a 200-km radius and stack the corresponding depth profiles to obtain a reflectivity estimate at the grid point. We will refer to the results as common-reflection-point (CRP) stacks. Note that there is considerable overlap in the sampling between adjacent grid points, as the 200-km CRP radius exceeds the grid point spacing, which naturally imposes some degree of spatial smoothing to our results. The nominal lateral resolution could be increased by reducing the cap radius, but this would lower the stack fold and reduce the signal-to-noise of the $P410P$ and $P660P$ reflections. We have not yet thoroughly explored these trade-offs, but a 200-km radius appears a reasonable compromise between resolution and fidelity for our data set.

3 RESULTS

Fig. 3 plots the average absolute value of the CRP stacks as a function of depth, with the bottom panel showing results for the entire data set at all station separation distances. In general, the average absolute amplitude decreases steadily with depth, most sharply in the uppermost mantle, and the 410- and 660-km reflectors appear as bumps overlain on this general trend. There are no other depths, at least below 200 km, that show obvious peaks, although there are hints of a possible peak near 270 km and a broader peak near 890 km. The overall decreasing amplitude with depth could be caused by incomplete time-domain removal of surface waves (which would have its strongest impact for the very upper mantle)

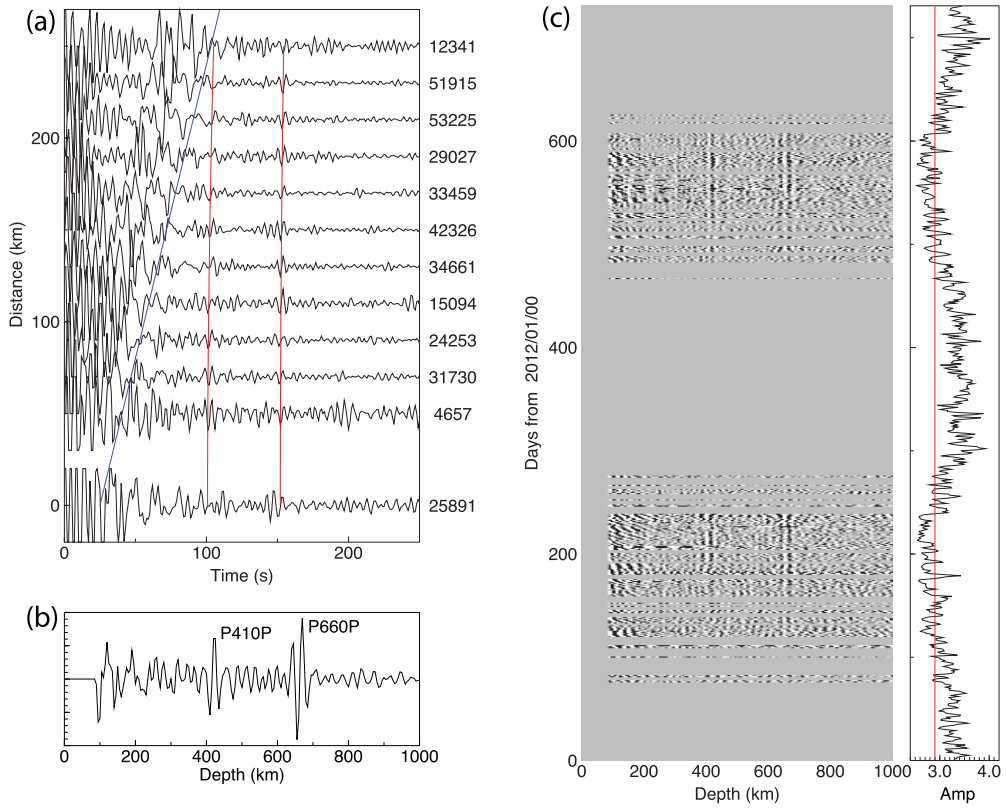

Figure 2. Similar to Fig. 1 but only using daily cross-correlation functions when the average daily log amplitude is less than 2.9, as shown by the vertical line in (c).

and the reduction in reflector amplitude expected from increased geometric spreading for deeper reflectors. However, it is also likely that much of the amplitude decrease with depth reflects stronger heterogeneity and/or layering in the shallow mantle, which results in greater seismic scattering. This interpretation is supported by the strong increase in heterogeneity within the top few hundred kilometres observed in mantle tomography models (e.g. Becker & Boschi 2002; French & Romanowicz 2014).

Fig. 3 also shows the overall results divided into different station separation distances. Both the 410- and 660-km reflector peaks are seen at station separations between 50 and 200 km. Only the 660 peak is seen beyond 200 km because the surface-wave arrival begins to overlap with $P4410P$ and is windowed out. Interestingly, single-station autocorrelation results do not show the 410- and 660-km reflector peaks. We will discuss possible reasons for this later, but exclude the autocorrelation results from the CRP stacks that are presented in the remainder of this paper. It should be noted that there are far more station pairs within our distance limits than there are individual stations, so excluding the autocorrelations removes only a small fraction of the total data set.

Results for the CRP caps are shown in west–east profile cross-sections at constant latitude in Figs 4 to 7. Caps are only plotted that contain at least 40 000 daily cross-correlation functions in their stack. Plotted amplitude is increased with depth in the plots as $(z/100)^{1.2}$, where z is depth in kilometres, to compensate for the generally lower amplitudes at deeper depths (as shown in Fig. 3). We do not show results at less than 200-km depth because of the increasingly limited data at shallow depths caused by our surface-wave exclusion cutoff (which causes a truncation artefact reflection at about 150-km depth) and our decision to exclude the autocorrelation functions. For reference, 3-D velocity perturbations from the tomography model of Boyce *et al.* (2023) are shown as background colours. Because topside reflections from positive impedance increases with depth should be negatively polarized compared to the direct P-wave arrivals (e.g. Shearer 1991), we flip the stack polarities and shade in black the negative parts of the traces to highlight expectations for $P410P$ and $P660P$ reflections. Examples of such clean negative-polarity pulses in Fig. 5 include the 660-km reflection in the 36°N profile near −85° longitude and the 410-km reflection in the 38°N profile near −117° longitude. However, in many areas the polarity of the discontinuity reflections appears unclear or even reversed compared to the negative-polarity pulses. This likely results from a combination of the relatively narrow band 0.1 to 0.3-Hz filter applied to the data, which produces 'ringy' waveforms, and incoherent stacking effects, that is, where discontinuity topography and/or time-shifts from 3-D velocity structure produce irregular pulse alignments and incoherent stacking.

Because of the nonlinear nature of our processing (time-dependent amplitude normalization of seismograms, nth root filtering applied to the cross-correlation functions), we retain no absolute amplitude information regarding the strength of the $P410P$ and $P660P$ reflections. However, because adjacent parts of the data set likely share similar signal-to-noise properties, the relative strength of reflections at nearby locations and depths should provide useful insights into discontinuity properties. Thus, for now we do not attempt to interpret discontinuity polarity or infer the size of impedance changes, and focus only on the depth and relative

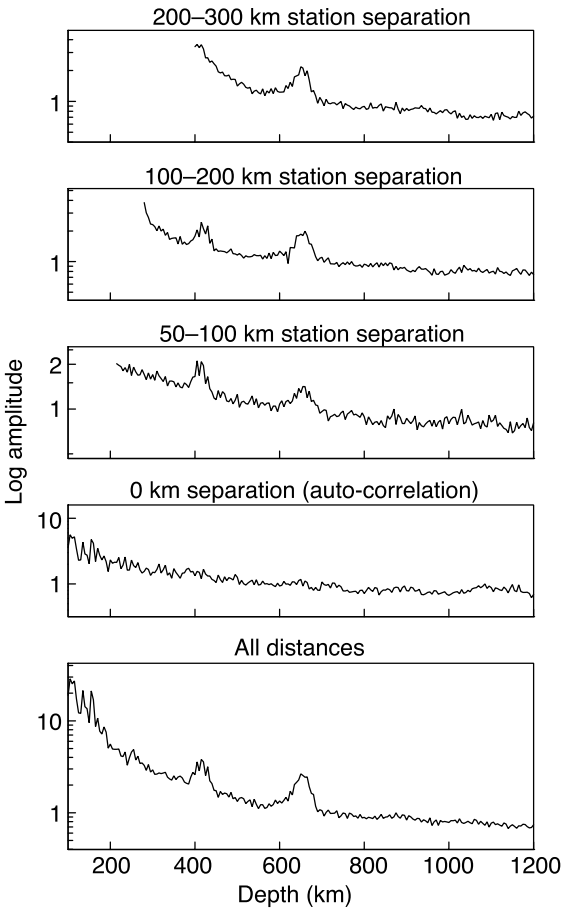

Figure 3. Average amplitude in the CRP stacks as a function of reflector depth. Results are shown for all station separation distances in the bottom panel, and for different station separation intervals in the top four panels.

visibility of the reflections. We also do not attempt to resolve discontinuity depth variations, which would require correcting the traveltimes for a specific 3-D velocity model, a complication we defer to future work.

Our results place some constraints on the sharpness of the discontinuities that generate the observed *P*-wave reflections. As noted by Richards (1972), near-vertical reflections for wavelength λ decrease rapidly when the gradient depth interval exceeds $\lambda/5$. For 5-s period waves this occurs at about 10-km thickness for the 410- and 660-km discontinuities. For our filtered data, about a 50 per cent reduction in refection amplitude occurs for a ∼15-km linear impedance gradient compared to a sharp discontinuity. Note that discontinuity topography within the CRP stacking region can produce a similar reduction in reflection amplitude because of incoherent stacking effects.

4 DISCUSSION AND CONCLUSIONS

Both the 410- and 660-km reflectors appear in the profiles of Figs 4 to 7, but the 660-km discontinuity is seen more clearly and more continuously. This contrasts with the recent *P*-wave ambient noise results of Chen *et al.* (2025) in northeast China and Zhang *et al.* (2025) in Japan, in which the 410-km reflector is imaged more strongly than the 660-km discontinuity. The Chen *et al.* (2025) and Zhang *et al.* (2025) studies applied a 0.1–0.2 Hz bandpass filter, compared to the 0.1–0.3 Hz filter used here; the inclusion of higher frequencies may reduce the relative visibility of the 410-km discontinuity assuming that it occurs over a broader depth range than the 660-km discontinuity. We do not see any widespread reflectors at depths other than 410 and 660 km, as is also indicated in Fig. 3. We also do not see apparent reflections from the Farallon Slab, although our CRP stacking approach assumes near-horizontal reflectors and will tend to suppress dipping features.

Many of the profiles suggest an association between strong 660-km reflections and faster regions in the Boyce *et al.* (2023) *P*-wave tomography model. Examples include the latitude 30° to 34° profiles near longitude −95° (Fig. 4), the latitude 35° to 38° profiles near longitude −85° (Fig. 5) and the latitude 41° to 42° profiles near longitude −97° (Fig. 6). To check this relationship more directly, Fig. 8 plots velocity perturbations at both 410 and 660 km from Boyce *et al.* (2023) versus our reflector peak amplitudes (taken from between 620 and 700 km depth). Although there is considerable scatter, a clear positive correlation is apparent at 660 km depth while no correlation is observed at 410 km.

To the extent that faster velocities in the Boyce *et al.* (2023) tomography model plotted here are related to subduction of the Farallon slab, a correlation with 660-reflector amplitude is opposite to that seen in global SS-precursor studies, in which lower *S*660*S* amplitudes are seen in subduction zones (Tauzin *et al.* 2022; Hao *et al.* 2024). These lower *S*660*S* amplitudes can be explained by assuming greater basalt enrichment in subduction zones compared to the surrounding mantle (e.g. Tauzin *et al.* 2022). Possible reasons for the apparent discrepancy in subduction zone 660-km reflection amplitudes warrant further study, but it should be noted that the SS precursor studies mainly sample the western Pacific subduction zones and are sensitive to *S* waves at longer periods than the *P* waves used here. In addition, as discussed below, more work is needed to validate details of the features seen in our *P* reflection profiles.

Other interesting features in our profiles include:

(i) Gaps in the 410 reflections and a lack of 660 reflections near latitude = 44°N, longitude = −109° (Fig. 6).
(ii) An apparent reflector near 500-km depth seen in the latitude = 43–44°N profiles near longitude = −106° (Fig. 6).
(iii) An apparent reflector near 480-km depth seen in the latitude = 31–32°N profiles near longitude = −87° (Fig. 4).

It is tempting to begin interpreting some of these features and relating them to tomography models and mantle dynamics. However, can we be sure these details are real and not caused by some kind of data- or processing-related artefact? Caution is warranted for the following reasons:

(i) The results show no clear agreement with previous MTZ studies using other methods. For example, the Gao & Liu (2014) USArray *P* receiver function study finds continuous 410- and 660-km discontinuities across the United States, without the gaps and large amplitude variations we see here. Fig. 9 compares amplitudes near 410, 520 and 660 km as imaged with *P*-wave noise cross-correlation (this study), top-side *SH*-wave reflections (Shearer & Buehler 2019) and *SS* precursors. Although the 520-km discontinuity does not appear as a distinctive feature in our results (see Fig. 3), we include its possible amplitudes in these maps to compare with other studies. There is little apparent correlation between the noise cross-correlation and the top-side *SH*-wave reflections, which were stacked over similar CRP bins. This lack of correlation with the top-side *SH* reflection amplitudes can be seen more directly in Fig. 10, which compares the amplitudes near 410 and 660-km at

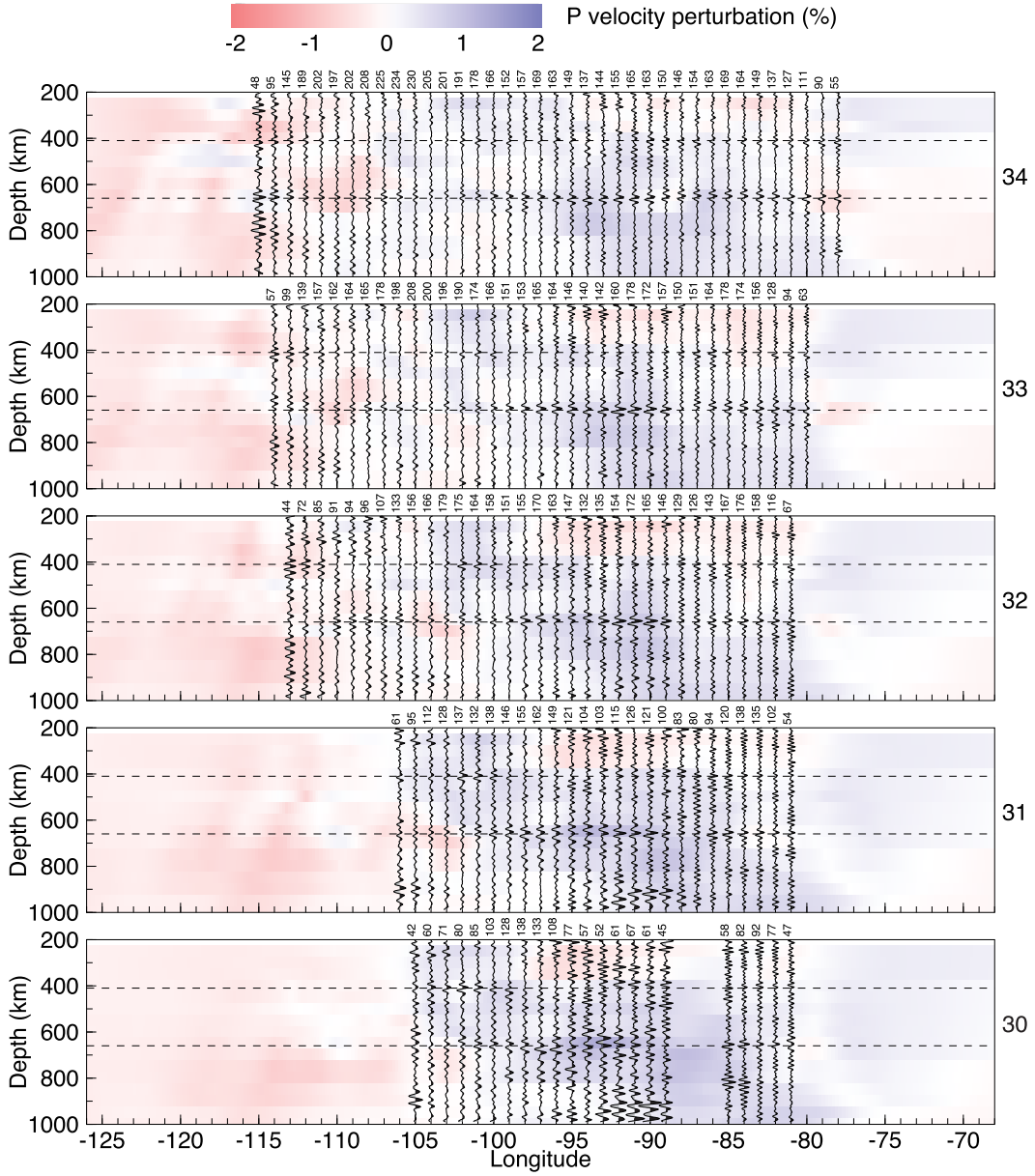

Figure 4. *P*d*P* reflection profiles from stacks of noise cross-correlations, plotted along lines of constant latitude from 30° to 34°N. Dashed lines show reference depths of 410 and 660 km. Background colours are from the tomography model of Boyce *et al.* (2023), with red and blue indicating slower and faster than average *P* velocity, respectively (see colour bar). The number of cross-correlations (in thousands) included in the CRP bin is labelled above each profile. Colors in the PDF version of this figure may not display correctly in some versions of the Mac Preview program.

the same CRP locations as our *P*-wave cross-correlations. The *SS* precursor amplitude results shown in Fig. 9 have much lower lateral resolution, but also do not show much agreement. Given differences among methods in frequency content, ray path geometry, data volumes and corrections in many cases for 3-D velocity structure, some disagreement in results for upper-mantle discontinuity topography and amplitudes should be expected. Thus, we do not mean to imply that any of the results plotted in Fig. 9 are wrong, only that more work is needed to understand the observed differences and what they imply for the true nature of the upper-mantle discontinuity structure under the United States.

(ii) Some CRP bins appear noisy at all depths and these higher amplitudes occur more often at the edges of array. For example, this is seen on the 30°N-latitude profile at −97° to −89° longitude, the 37°N-latitude profile at −120 to −115° longitude and in the 49°N-latitude profile near −105° longitude. These features are not simply related to smaller numbers of CRP bouncepoints in the stacks.

(iii) In principle, there should be source-side reflections from upper-mantle discontinuities, which will arrive at the same times as the receiver-side reflections, an issue discussed by Shearer & Buehler (2019) for topside *SH*-wave reflections from teleseisms recorded by USArray stations. This complicates interpreting imaged features solely in terms of receiver-side structure.

Aiman *et al.* (2025b, a) recently identified and mapped mantle reflectors under the contiguous United States in *P*-wave ambient noise cross-correlation analyses that have many similarities to our

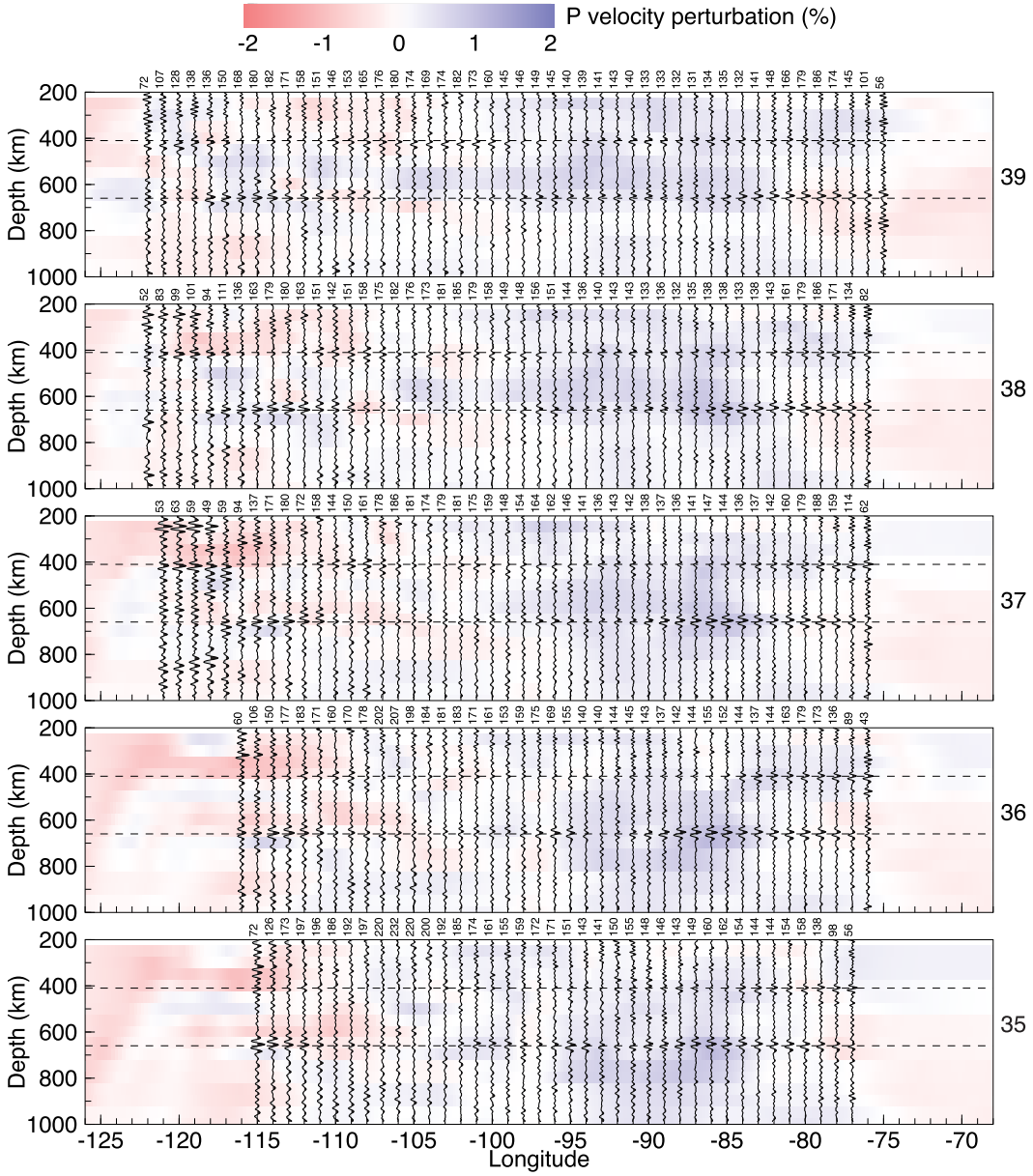

Figure 5. *P*d*P* reflection profiles from stacks of noise cross-correlations, plotted along lines of constant latitude from 35° to 39°N. Dashed lines show reference depths of 410 and 660 km. Background colours are from the tomography model of Boyce *et al.* (2023), with red and blue indicating slower and faster than average *P* velocity, respectively (see colour bar). The number of cross-correlations (in thousands) included in the CRP bin is labelled above each profile. Colors in the PDF version of this figure may not display correctly in some versions of the Mac Preview program.

study. The main differences are: (1) They supplemented the USArray TA stations with 356 permanent stations; (2) They used time windows with low H/V ratios (e.g. Pedersen *et al.* 2023) rather than the noise amplitude criteria applied here; (3) They used station pairs with separation distances of 40 to 180 km (compared to our use of 50 to 300 km); (4) They stacked correlation data from station pairs within 400 km radius of each model grid point, which provides more intrinsic smoothing than the 200-km radius that we employ in our common-reflection point approach, although they also downweight data at greater distances, increasing their effective resolution; (5) They correct traveltimes for the 3-D velocity model US-SL-2014 (Schmandt & Lin 2014); and (6) They discard individual noise cross-correlation functions that have correlation coefficients with the stack less than 0.1.

We have not attempted a detailed comparison of our results to these studies. However, Fig. 3(c) from Aiman *et al.* (2025b) shows a profile at 40°N latitude that can be directly compared with the same latitude in Fig. 6. In general, the Aiman *et al.* (2025b) 410- and 660-km reflectors appear much smoother and more continuous than is seen in our profile at the same latitude, which has gaps in the 410-km reflector near −115 and −98 degree longitude. We do not fully understand the origin of these differences, but the greater lateral smoothing and the discarding of cross-correlation functions that do not fit the final result in Aiman *et al.* (2025b) likely both play important roles. The data selection procedure has a significant effect, as the 520-km discontinuity is not apparent in Fig. 3(c) from Aiman *et al.* (2025b), whereas it is seen strongly in the 520-km discontinuity focused study of Aiman *et al.* (2025a), which used

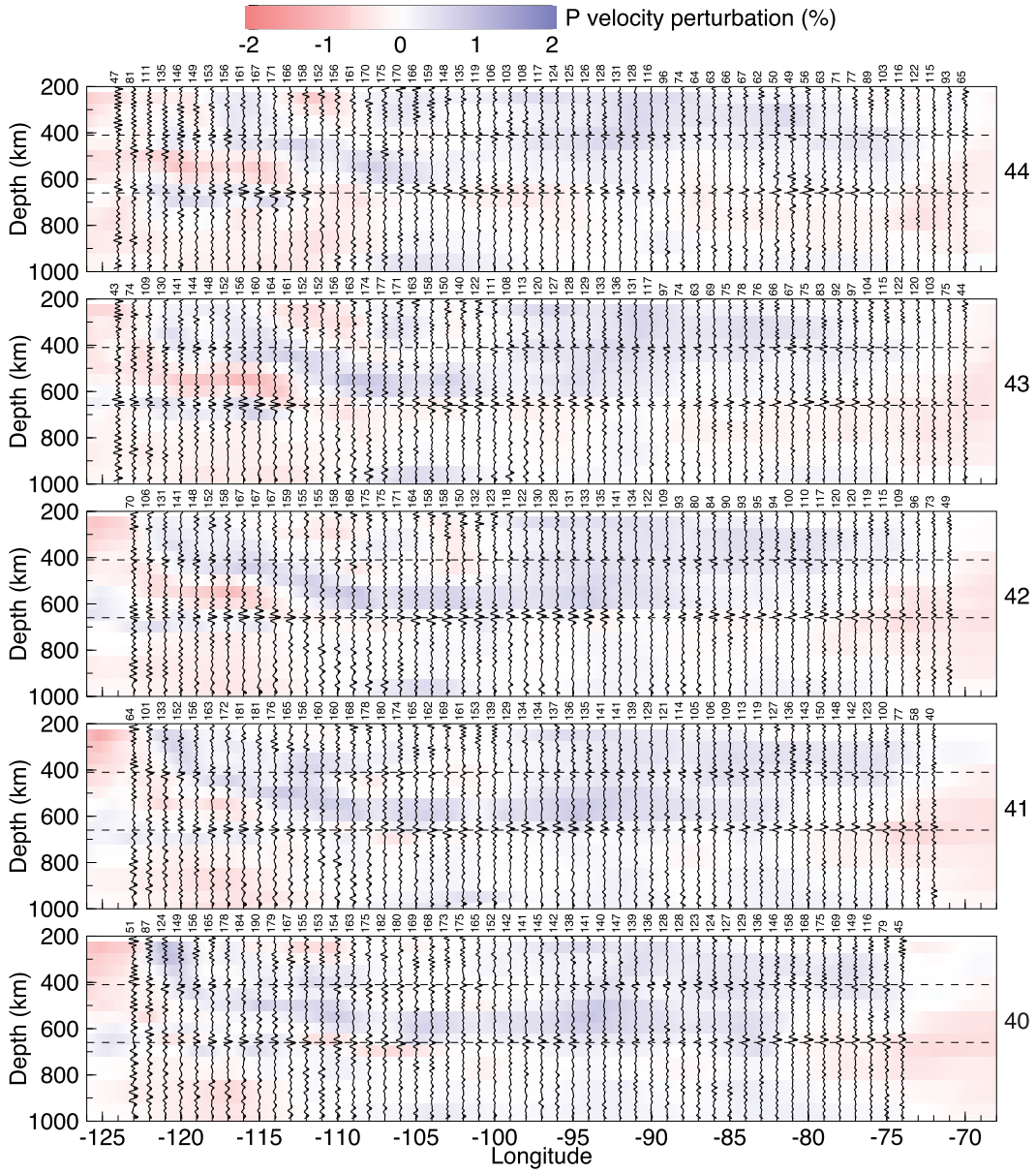

Figure 6. *P*d*P* reflection profiles from stacks of noise cross-correlations, plotted along lines of constant latitude from 40° to 44°N. Dashed lines show reference depths of 410 and 660 km. Background colours are from the tomography model of Boyce *et al.* (2023), with red and blue indicating slower and faster than average *P* velocity, respectively (see colour bar). The number of cross-correlations (in thousands) included in the CRP bin is labelled above each profile. Colors in the PDF version of this figure may not display correctly in some versions of the Mac Preview program.

only cross-correlations with greater than 0.1 correlation coefficient with the final stack just within a narrow time window of the expected 520-km reflection.

Thus, while it is clear that 410- and 660-km reflections are observed in our noise cross-correlation results for many locations, more research will be required to understand and reliably interpret the variability seen in the CRP profiles of Figs 4 to 7. Ambient noise methods recover an unbiased estimate of the station-to-station Green's function when there exists a reasonably well-distributed set of noise sources (Tsai 2009), such that only sources along the 'correct' ray path sum constructively (we use 'correct' to refer to the upcoming ray path aligned with the station-to-station Green's function ray path). A strong noise source from a single location away from the correct ray path may yield erroneous cross-correlation peaks if not enough noise sources are present from nearby locations for destructive interference to occur (because the traveltime and phase change with respect to differences in source location except for the stationary phase point at the correct ray path geometry). In our case, this could result in a reflection from the 410- or 660-km discontinuity being assigned an incorrect depth in our analysis. Another possible artefact is 'cross terms' arising from different body wave phases (e.g. *P* and *PP*) from a persistently active source region (Pedersen & Colombi 2018).

Beam forming results have shown that *P*-wave noise sources are often generated by oceanic storms (e.g. Gerstoft *et al.* 2008; Landès *et al.* 2010; Pandey *et al.* 2024) that are localized in time and space. *P*-wave microseism noise recorded at global seismic stations was back-projected by Zhang *et al.* (2023) to map source

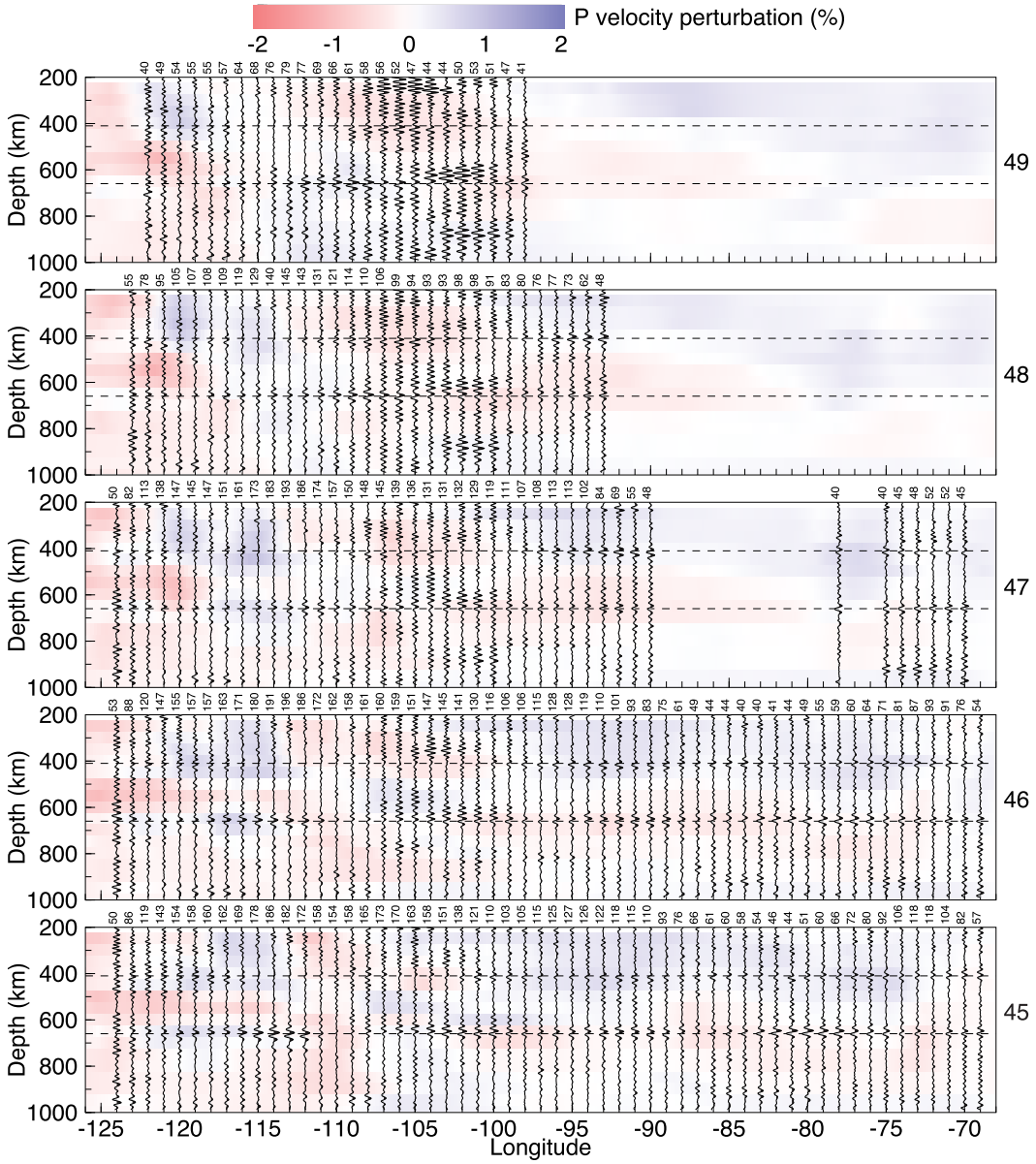

Figure 7. *P*d*P* reflection profiles from stacks of noise cross-correlations, plotted along lines of constant latitude from 45° to 49°N. Dashed lines show reference depths of 410 and 660 km. Background colours are from the tomography model of Boyce *et al.* (2023), with red and blue indicating slower and faster than average *P* velocity, respectively (see colour bar). The number of cross-correlations (in thousands) included in the CRP bin is labelled above each profile. Colors in the PDF version of this figure may not display correctly in some versions of the Mac Preview program.

locations during 2015 and 2020. The noise sources are highly heterogeneous, with some oceanic locations appearing much more energetic than surrounding regions. This suggests that non-uniform noise sources may well be an issue for global *P*-wave ambient noise cross-correlation studies, an issue recently discussed by Li *et al.* (2020a, b).

To gain some insight regarding the likely location of noise sources for our USArray analysis, Fig. 11 shows points 180° away from the station locations (i.e. at the antipodes). Results from Zhang *et al.* (2023) suggest that the strongest noise sources in the Indian Ocean are at latitudes between 40°S and 60°S, as shown by the dashed lines in the figure. Note that only antipodes from the northern USArray stations are within this zone, which may at least partially explain why we do not see 410- and 660-km reflections in the averaged autocorrelation data, which require noise sources directly below the stations. Another factor may be that PKP amplitudes at 180° (i.e. on the DF branch) have lower amplitudes than other parts of PKP. The $PKP(BC)$ branch is particularly bright and occurs at 145° to 155° distance. For reference, Fig. 11 shows points located 150° away from USArray stations. Note that many of these points are within the zone of expected noise sources, but the coverage is likely to be far from isotropic. $PKP(BC)$ has an expected slowness increasing from 2.20 s deg^{-1} at 154° distance to 3.07 s deg^{-1} at 146° distance (Kennett & Engdahl 1991). These slownesses align with those predicted for the surface-to-surface *P*-wave reflection for the 410-km discontinuity at station separation distances of about 130 to 200 km and for the 660-km discontinuity at separation distances of about 170 to 380 km.

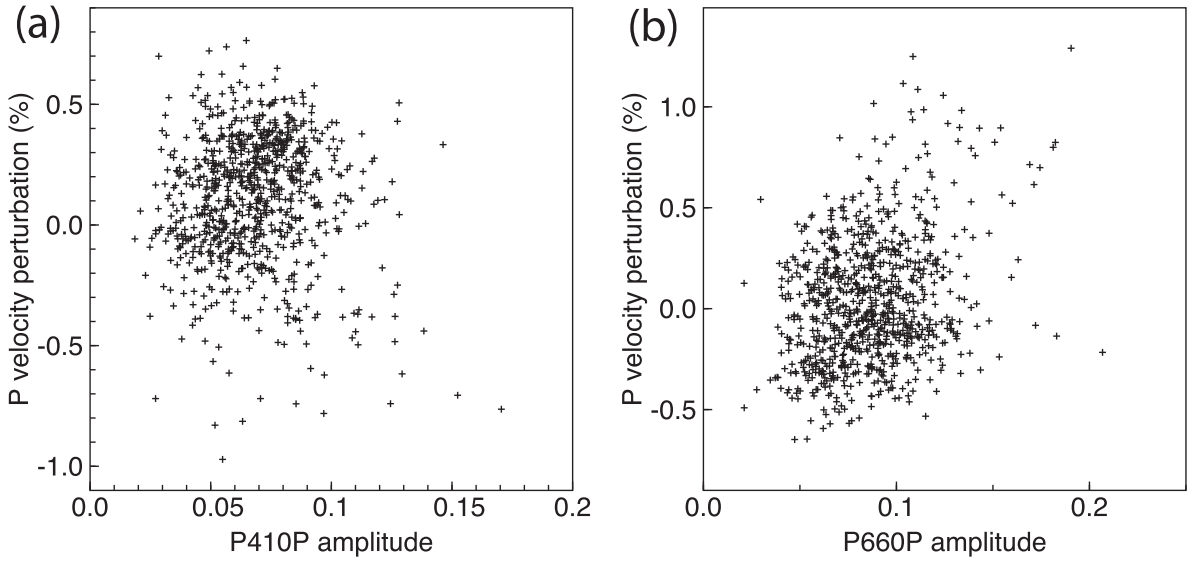

Figure 8. Tomographic *P*-wave velocity perturbation from Boyce *et al.* (2023) versus (a) 410-km reflector amplitude, and (b) 660-km reflector amplitude from our noise cross-correlation analysis.

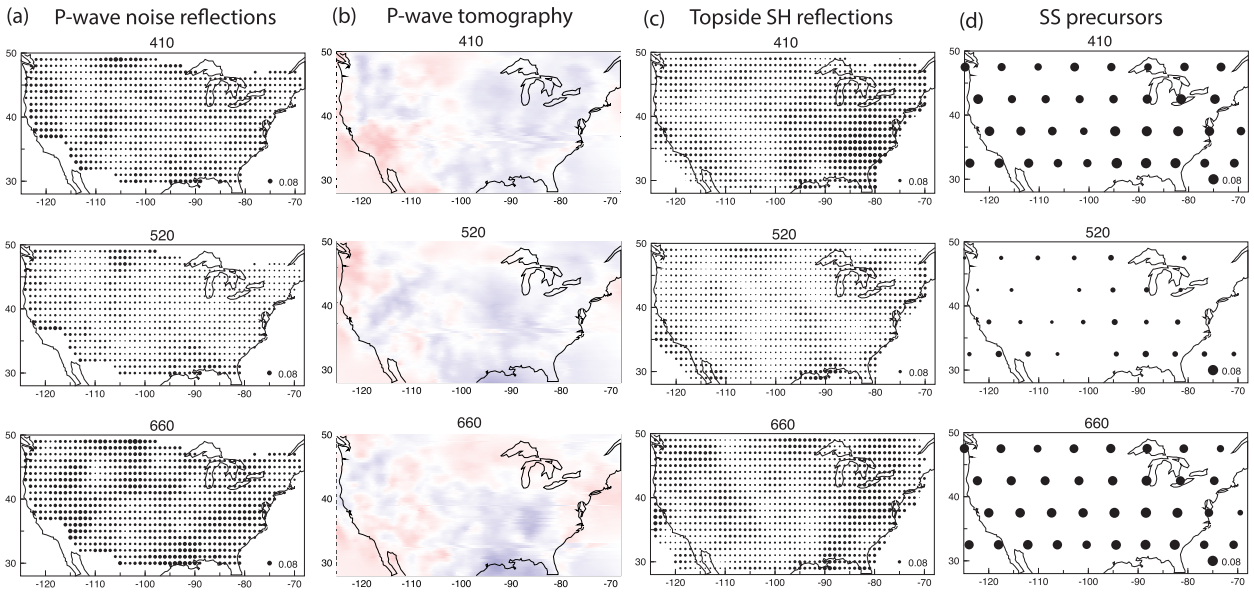

Figure 9. A comparison of average amplitudes of the 410, 520 and 660-km discontinuities measured by different methods and the *P*-wave tomography model of Boyce *et al.* (2023) at the same depths. In (a), (c) and (d), the reflection amplitudes are plotted at the centre of their CRP bins. The area of each circle is proportional to the average absolute value of the stack amplitude between 390 and 430 km for the '410', 480 and 560 km for the '520', and 630 and 690 km for the '660.' A reference amplitude of 0.08 is plotted at the lower right of each panel. (a) The *P*-wave noise cross-correlation results from this study. (b) *P*-wave velocity perturbations from Boyce *et al.* (2023), with faster velocities in blue and slower velocities in red (see Fig. 7 for colour scale). (c) Topside *SH* reflections from Shearer & Buehler (2019). (d) *SS* precursors normalized by *SS* amplitudes in circular caps with 5° spacing and 10° radius from Tian *et al.* (2020). Colors in the PDF version of this figure may not display correctly in some versions of the Mac Preview program.

The observed amplitude of Indian Ocean noise sources at USArray stations will depend both on the strength of the source and its distance, in particular whether it lies with the $\sim 145^\circ$ to 155° range for $PKP(BC)$ arrivals. Thus, we can expect both the orientation and amplitude of the upcoming *P*-wave microseisms to be highly heterogeneous in both time and space. However, in principle this heterogeneity can be mapped using beamforming or back-projection approaches (e.g. Gerstoft *et al.* 2008; Landès *et al.* 2010; Zhang *et al.* 2023; Pandey *et al.* 2024) and could be taken into account when interpreting noise cross-correlation results for mantle discontinuity mapping. For example, daily beamforming with sub-arrays could be performed to identify spatially compact noise sources, with ray tracing then used to map any observed top-side reflections to the correct location and depth. Such analyses could also search for cross-term contamination from different body wave phases, such as those observed to interfere with *P*-wave reflections from the 410-km discontinuity by Pedersen & Colombi (2018). A recent detailed synthetic analysis by Pawlowski *et al.* (2025) of topside 410- and

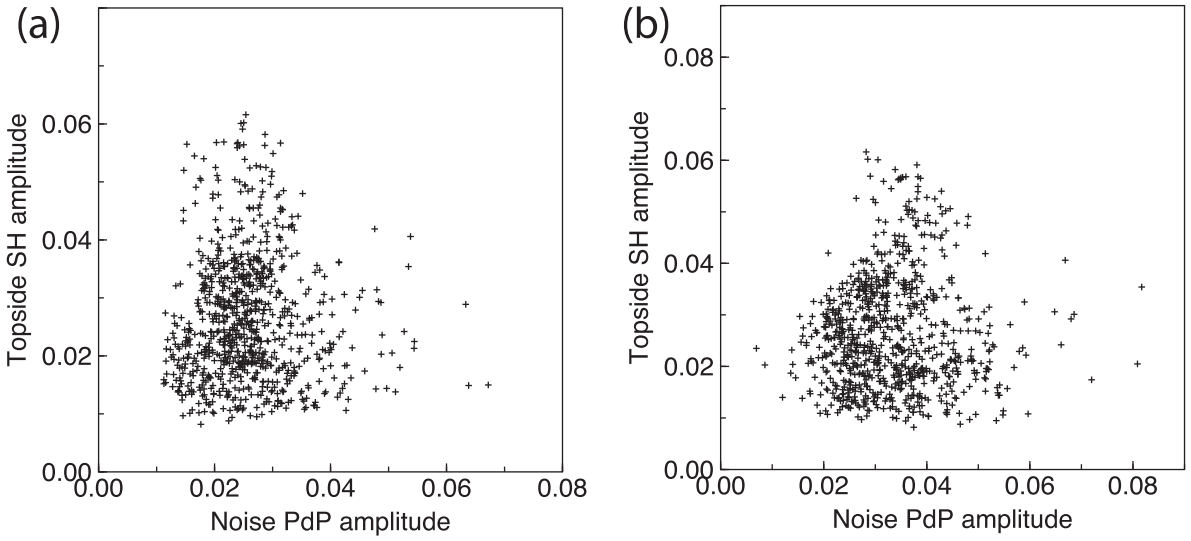

Figure 10. Top-side *SH*-wave reflection amplitudes from Shearer & Buehler (2019) versus (a) 410-km reflector amplitude, and (b) 660-km reflector amplitude from our noise cross-correlation analysis. Note the lack of correlation.

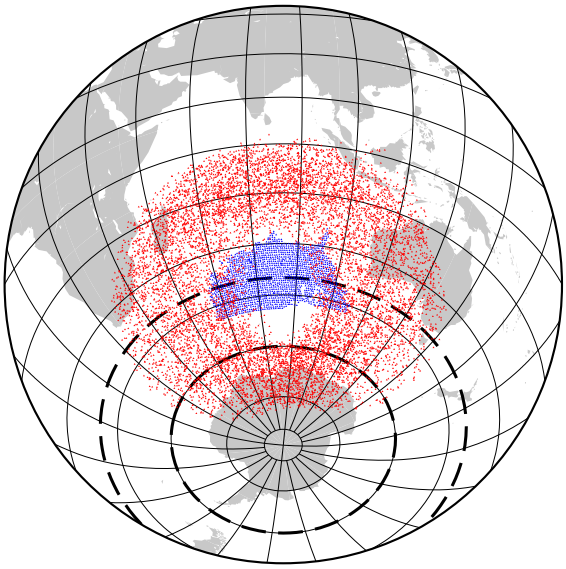

Figure 11. A map showing that USArray station antipodes (plotted in blue) are located in the Indian Ocean. The red points show 10 000 locations 150° away from USArray stations at random azimuths, which should sample the relatively bright $PKP(BC)$ phase. The heavy dashed lines are at latitudes of 40° and 60°S, which bracket the strongest noise sources mapped by Zhang *et al.* (2023) in the Indian Ocean.

660-km *P*-wave reflections in noise cross-correlation results highlighted the important role of the b-caustic of the $PKP(BC)$ branch and showed that selecting favourable source conditions can reduce biases in true station-to-station Green's function recovery.

The problem of distinguishing source-side and receiver-side reflections in *P*-wave noise cross-correlation data deserves more attention, as Earth's microseism noise sources all occur at the surface. As discussed by Shearer & Buehler (2019) in an analysis of top-side *S*-wave reflections from distant earthquakes observed at USArray stations, the nearly universal global presence of the 410- and 660-km discontinuities makes it difficult to separate source- and receiver-side contributions to observed reflections because it cannot be assumed that the source-side reflections from different source locations will destructively interfere. However, the shorter periods of the *P*-wave reflections in noise cross-correlation data compared to the longer period *S*-wave reflections in Shearer & Buehler (2019) makes it more likely that the source-side reflections will cancel out, given some degree of source-side discontinuity depth and/or 3-D upper-mantle velocity variations. In addition, as argued by Pawlowski *et al.* (2025), the differing station locations on the receiver side will have a similar effect as an extended source in terms of cancelling the unwanted cross-terms in cross-correlation results.

None of these possible complications should distract from our main result—that *P*-wave reflections from the 410- and 660-km discontinuities are readily visible in stacks of ambient noise cross-correlation functions from USArray stations across the contiguous United States. This is consistent with other recent *P*-wave ambient noise studies (e.g. Poli *et al.* 2012a; Feng *et al.* 2017, 2021, 2022; Pedersen *et al.* 2023; Aiman *et al.* 2025b; Chen *et al.* 2025; Zhang *et al.* 2025) and opens up new approaches to studying transition zone structure. Encouragingly, discontinuity reflections are seen in common reflection point stacks within caps of 200-km radius over limited time periods (typically one to two seasons of northern-hemisphere summer months when the ambient *P* waves have the best signal-to-noise), suggesting that mapping lateral variations in mantle discontinuities is possible given suitable station coverage. The observed *P*-wave reflections are primarily sensitive to the *P*-wave impedance contrast across the discontinuities, making them a useful complement to receiver function studies, which are mainly sensitive to the *S*-velocity contrast (e.g. Rychert *et al.* 2007). They are also observed at relatively short periods (3 to 10) and have greater intrinsic vertical resolution than receiver function studies or *PP* precursor studies (e.g. Deuss *et al.* 2006; Waszek *et al.* 2021; Yu *et al.* 2023). Thus, ambient noise topside *P*-wave reflections have great potential to improve our understanding of mantle discontinuities, as evidenced by the detailed reflection profiles presented here, although further work is required to unravel the effects of non-uniform noise sources on the cross-correlation results.

ACKNOWLEDGMENTS

This research was made possible by the support of National Science Foundation grants EAR-2123529 and EAR-2147923. CAR was supported by NSF-EAR-2147918, NSF-OCE-2316136 and NSF-EAR 2333101. SSW was supported by the MSU Geological Endowment.

DATA AVAILABILITY

Seismic data from the USArray experiment are freely available to the public from the EarthScope/IRIS Data Management Center (https://ds.iris.edu/ds/nodes/dmc/) funded by the National Science Foundation, under Cooperative Agreement EAR-1851048.

REFERENCES

Aiman, Y.A., Lu, Y., Estève, C. & Bokelmann, G., 2025a. Internal structure of the mantle transition zone beneath the contiguous US: insights from the 520-km discontinuity revealed by ambient noise correlations, *Geophys. Res. Lett.,* **52**(8), e2025GL115453, doi:10.1029/2025GL115453.

Aiman, Y.A., Lu, Y., Esteve, C. & Bokelmann, G., 2025b. Mapping deep earth interfaces using noise correlations: a step-like mantle transition zone arrangement beneath the contiguous United States, *Seismol. Res. Lett.,* **96**(4), 2566–2576.

Babikoff, J.C. & Dalton, C.A., 2019. Long-period Rayleigh wave phase velocity tomography using usarray, *Geochem. Geophys. Geosyst.,* **20**(4), 1990–2006.

Becker, T.W. & Boschi, L., 2002. A comparison of tomographic and geodynamic mantle models, *Geochem. Geophys. Geosyst.,* **3**(1), doi:10.1029/2001GC000168.

Bensen, G., Ritzwoller, M. & Shapiro, N.M., 2008. Broadband ambient noise surface wave tomography across the United States, *J. geophys. Res.: Solid Earth,* **113**(B5), doi:10.1029/2007JB005248.

Bissig, F., Khan, A., Tauzin, B., Sossi, P.A., Munch, F.D. & Giardini, D., 2021. Multifrequency inversion of Ps and Sp receiver functions: methodology and application to USArray data, *J. geophys. Res.: Solid Earth,* **126**(2), e2020JB020350, doi:10.1029/2020JB020350.

Boué, P., Poli, P., Campillo, M., Pedersen, H., Briand, X. & Roux, P., 2013. Teleseismic correlations of ambient seismic noise for deep global imaging of the Earth, *J. geophys. Int.,* **194**(2), 844–848.

Boyce, A. *et al.*, 2023. A new P-wave tomographic model (CAP22) for North America: Implications for the subduction and cratonic metasomatic modification history of western Canada and Alaska, *J. geophys. Res.: Solid Earth,* **128**(3), e2022JB025745, doi:10.1029/2022JB025745.

Burdick, S. & Lekić, V., 2017. Velocity variations and uncertainty from transdimensional *P*-wave tomography of North America, *J. geophys. Int.,* **209**(2), 1337–1351.

Burdick, S. *et al.*, 2017. Model update may 2016: Upper-mantle heterogeneity beneath North America from travel-time tomography with global and USArray data, *Seismol. Res. Lett.,* **88**(2A), 319–325.

Burky, A.L., Irving, J.C. & Simons, F.J., 2023. The mantle transition zone beneath eastern North America: Receiver functions and tomographic velocity models, *Phys. Earth planet. Inter.,* **340,** 107035, doi:10.1016/j.pepi.2023.107035.

Campillo, M. & Paul, A., 2003. Long-range correlations in the diffuse seismic coda, *Science,* **299**(5606), 547–549.

Cao, A. & Levander, A., 2010. High-resolution transition zone structures of the Gorda Slab beneath the western United States: Implication for deep water subduction, *J. geophys. Res.: Solid Earth,* **115**(B7), doi:10.1029/2009JB006876.

Carr, S.A., Olugboji, T., Park, J. & Karato, S.i., 2025. High-resolution mapping of North America suggests numerous low-velocity zones above and below the mantle transition zone, *Tectonophysics,* **908,** 230775, doi:10.1016/j.tecto.2025.230775.

Chen, S., Yang, F., Wang, W., Zhang, L., Chen, Q.F. & Li, J., 2025. Lateral variations in upper mantle discontinuities beneath Northeast China revealed by seismic ambient noise, *J. geophys. Res.: Solid Earth,* **130**(5), e2024JB030624, doi:10.1029/2024JB030624.

Deuss, A., Redfern, S.A., Chambers, K. & Woodhouse, J.H., 2006. The nature of the 660-kilometer discontinuity in earth's mantle from global seismic observations of pp precursors, *Science,* **311**(5758), 198–201.

Feng, J., Yao, H., Poli, P., Fang, L., Wu, Y. & Zhang, P., 2017. Depth variations of 410 km and 660 km discontinuities in eastern North China Craton revealed by ambient noise interferometry, *Geophys. Res. Lett.,* **44**(16), 8328–8335.

Feng, J., Yao, H., Wang, Y., Poli, P. & Mao, Z., 2021. Segregated oceanic crust trapped at the bottom mantle transition zone revealed from ambient noise interferometry, *Nat. Commun.,* **12**(1), 2531, doi:10.1038/s41467-021-22853-2.

Feng, J., Yao, H., Chen, L. & Wang, W., 2022. Massive lithospheric delamination in southeastern Tibet facilitating continental extrusion, *Nat. Sci. Rev.,* **9**(4), nwab174, doi:10.1093/nsr/nwab174.

French, S. & Romanowicz, B.A., 2014. Whole-mantle radially anisotropic shear velocity structure from spectral-element waveform tomography, *J. geophys. Int.,* **199**(3), 1303–1327.

Gao, S.S. & Liu, K.H., 2014. Mantle transition zone discontinuities beneath the contiguous United States, *J. geophys. Res.: Solid Earth,* **119**(8), 6452–6468.

Gerstoft, P., Shearer, P.M., Harmon, N. & Zhang, J., 2008. Global P, PP, and PKP wave microseisms observed from distant storms, *Geophys. Res. Lett.,* **35**(23), doi:10.1029/2008GL036111.

Golos, E. *et al.*, 2018. Shear wave tomography beneath the united states using a joint inversion of surface and body waves, *J. geophys. Res.: Solid Earth,* **123**(6), 5169–5189.

Hao, S., Wei, S.S. & Shearer, P.M., 2024. Substantial global radial variations of basalt content near the 660-km discontinuity, *AGU Adv.,* **5**(6), e2024AV001409, doi:10.1029/2024AV001409.

Hopper, E. & Fischer, K.M., 2018. The changing face of the lithosphere-asthenosphere boundary: Imaging continental scale patterns in upper mantle structure across the contiguous US with Sp converted waves, *Geochem. Geophys. Geosyst.,* **19**(8), 2593–2614.

Iris, T.A., 2003. USArray transportable array, *International Federation of Digital Seismograph Networks, Dataset/Seismic Network.*

Kanasewich, E., Hemmings, C. & Alpaslan, T., 1973. Nth-root stack nonlinear multichannel filter, *Geophysics,* **38**(2), 327–338.

Kennett, B. & Engdahl, E., 1991. Traveltimes for global earthquake location and phase identification, *J. geophys. Int.,* **105**(2), 429–465.

Kind, R., Yuan, X., Mechie, J. & Sodoudi, F., 2015. Structure of the upper mantle in the north-western and central united states from USArray S-receiver functions, *Solid Earth,* **6**(3), 957–970.

Landès, M., Hubans, F., Shapiro, N.M., Paul, A. & Campillo, M., 2010. Origin of deep ocean microseisms by using teleseismic body waves, *J. geophys. Res.: Solid Earth,* **115**(B5), doi:10.1029/2009JB006918.

Li, L., Boué, P. & Campillo, M., 2020a. Observation and explanation of spurious seismic signals emerging in teleseismic noise correlations, *Solid Earth,* **11**(1), 173–184.

Li, L., Boué, P., Retailleau, L. & Campillo, M., 2020b. Spatiotemporal correlation analysis of noise-derived seismic body waves with ocean wave climate and microseism sources, *Geochem. Geophys. Geosyst.,* **21**(9), e2020GC009112, doi:10.1029/2020GC009112.

Li, S., Huang, J., Liu, Z. & Zhang, Y., 2019. Study on the mantle discontinuity structures beneath Northeast China with time–frequency phase-weighted stacks of ambient noise correlations, *J. geophys. Int.,* **218**(3), 1490–1501.

Lin, F.C., Moschetti, M.P. & Ritzwoller, M.H., 2008. Surface wave tomography of the western United States from ambient seismic noise: Rayleigh and Love wave phase velocity maps, *J. geophys. Int.,* **173**(1), 281–298.

Lin, F.C., Ritzwoller, M.H. & Snieder, R., 2009. Eikonal tomography: surface wave tomography by phase front tracking across a regional broadband seismic array, *J. geophys. Int.,* **177**(3), 1091–1110.

Lin, F.C., Tsai, V.C., Schmandt, B., Duputel, Z. & Zhan, Z., 2013. Extracting seismic core phases with array interferometry, *Geophys. Res. Lett.,* **40**(6), 1049–1053.

Liu, T. & Shearer, P.M., 2021. Complicated lithospheric structure beneath the contiguous us revealed by teleseismic S-reflections, *J. geophys. Res.: Solid Earth,* **126**(5), e2020JB021624, doi:10.1029/2020JB021624.

Lu, Y., Pedersen, H.A., Stehly, L. & Group, A.W., 2022. Mapping the seismic noise field in Europe: spatio-temporal variations in wavefield composition and noise source contributions, *J. geophys. Int.,* **228**(1), 171–192.

Luo, Y., Long, M.D., Rondenay, S., King, S.D., Mazza, S.E. & Wolf, J., 2025. Mantle transition zone-penetrating upwellings beneath the eastern North American margin and beyond, *J. geophys. Res.: Solid Earth,* **130**(4), e2024JB030005, doi:10.1029/2024JB030005.

Meltzer, A. *et al.*, 1999. The USArray initiative, *Geol. Soc. Am. Today,* **9,** 8–10.

Nishida, K., 2013. Global propagation of body waves revealed by cross-correlation analysis of seismic hum, *Geophys. Res. Lett.,* **40**(9), 1691–1696.

Obrebski, M., Allen, R.M., Xue, M. & Hung, S.H., 2010. Slab-plume interaction beneath the Pacific Northwest, *Geophys. Res. Lett.,* **37**(14), doi:10.1029/2010GL043489.

Obrebski, M., Allen, R.M., Pollitz, F. & Hung, S.H., 2011. Lithosphere–asthenosphere interaction beneath the western United States from the joint inversion of body-wave traveltimes and surface-wave phase velocities, *J. geophys. Int.,* **185**(2), 1003–1021.

Pandey, A., Tkalčić, H. & Ma, X., 2024. Investigating the characteristics of microseisms using the Australian seismic arrays, *J. geophys. Res.: Solid Earth,* **130,** doi:10.1029/2024JB031032.

Paul, A., Campillo, M., Margerin, L., Larose, E. & Derode, A., 2005. Empirical synthesis of time-asymmetrical Green functions from the correlation of coda waves, *J. geophys. Res.: Solid Earth,* **110**(B8), doi:10.1029/2004JB003521.

Pawlowski, P., Pedersen, H., Boué, P., Tauzin, B. & Tomasetto, L., 2025. Modelling *P* wave reflections on MTZ discontinuities from distant oceanic sources, *J. geophys. Int.,* **242**(3), ggaf275, doi:10.1093/gji/ggaf275.

Pedersen, H. & Colombi, A., 2018. Body waves from a single source area observed in noise correlations at arrival times of reflections from the 410 discontinuity, *J. geophys. Int.,* **214**(2), 1125–1135.

Pedersen, H.A., Mattern, F., Poli, P. & Stehly, L., 2023. Imaging with seismic noise: improving extraction of body wave phases from the deep Earth through selective stacking based on H/V ratios, *J. geophys. Int.,* **232**(2), 1455–1467.

Poli, P., Campillo, M., Pedersen, H. & Group, L.W., 2012a. Body-wave imaging of Earth's mantle discontinuities from ambient seismic noise, *Science,* **338**(6110), 1063–1065.

Poli, P., Pedersen, H. & Campillo, M., 2012b. Emergence of body waves from cross-correlation of short period seismic noise, *J. geophys. Int.,* **188**(2), 549–558.

Porritt, R.W., Allen, R.M. & Pollitz, F.F., 2014. Seismic imaging east of the Rocky Mountains with USArray, *Earth planet. Sci. Lett.,* **402,** 16–25.

Richards, P.G., 1972. Seismic waves reflected from velocity gradient anomalies within the Earth's upper mantle, *J. Geophys.,* **38,** 517–527.

Rychert, C.A., Rondenay, S. & Fischer, K.M., 2007. *P*-to-*S* and *S*-to-*P* imaging of a sharp lithosphere-asthenosphere boundary beneath eastern North America, *J. geophys. Res.: Solid Earth,* **112**(B8), doi:10.1029/2006JB004619.

Schimmel, M. & Paulssen, H., 1997. Noise reduction and detection of weak, coherent signals through phase-weighted stacks, *J. geophys. Int.,* **130**(2), 497–505.

Schmandt, B. & Humphreys, E., 2010. Complex subduction and small-scale convection revealed by body-wave tomography of the western United States upper mantle, *Earth planet. Sci. Lett.,* **297**(3–4), 435–445.

Schmandt, B. & Lin, F.C., 2014. P and S wave tomography of the mantle beneath the United States, *Geophys. Res. Lett.,* **41**(18), 6342–6349.

Schmandt, B., Jacobsen, S.D., Becker, T.W., Liu, Z. & Dueker, K.G., 2014. Dehydration melting at the top of the lower mantle, *Science,* **344**(6189), 1265–1268.

Shearer, P.M., 1991. Constraints on upper mantle discontinuities from observations of long-period reflected and converted phases, *J. geophys. Res.: Solid Earth,* **96**(B11), 18147–18182.

Shearer, P.M. & Buehler, J., 2019. Imaging upper-mantle structure under USArray using long-period reflection seismology, *J. geophys. Res.: Solid Earth,* **124**(9), 9638–9652.

Sigloch, K., 2011. Mantle provinces under North america from multi-frequency P wave tomography, *Geochem. Geophys. Geosyst.,* **12**(2), doi:10.1029/2010GC003421.

Tauzin, B., Waszek, L., Ballmer, M.D., Afonso, J.C. & Bodin, T., 2022. Basaltic reservoirs in the Earth's mantle transition zone, *Proc. Natl Acad. Sci.,* **119**(48), e2209399119, doi:10.1073/pnas.2209399119.

Tian, D., Lv, M., Wei, S.S., Dorfman, S.M. & Shearer, P.M., 2020. Global variations of Earth's 520-and 560-km discontinuities, *Earth planet. Sci. Lett.,* **552,** 116600, doi:10.1016/j.epsl.2020.116600.

Tsai, V.C., 2009. On establishing the accuracy of noise tomography travel-time measurements in a realistic medium, *J. geophys. Int.,* **178**(3), 1555–1564.

Waszek, L., Tauzin, B., Schmerr, N.C., Ballmer, M.D. & Afonso, J.C., 2021. A poorly mixed mantle transition zone and its thermal state inferred from seismic waves, *Nat. Geosci.,* **14**(12), 949–955.

Yang, Y. & Ritzwoller, M.H., 2008a. Characteristics of ambient seismic noise as a source for surface wave tomography, *Geochem. Geophys. Geosyst.,* **9**(2), doi:10.1029/2007GC001814.

Yang, Y. & Ritzwoller, M.H., 2008b. Teleseismic surface wave tomography in the western US using the Transportable Array component of USArray, *Geophys. Res. Lett.,* **35**(4), doi: 10.1029/2007GL032278.

Yang, Y., Shen, W. & Ritzwoller, M.H., 2011. Surface wave tomography on a large-scale seismic array combining ambient noise and teleseismic earthquake data, *Earthq. Sci.,* **24,** 55–64.

Yu, C., Goes, S., Day, E.A. & van der Hilst, R.D., 2023. Seismic evidence for global basalt accumulation in the mantle transition zone, *Sci. Adv.,* **9**(22), eadg0095, doi:10.1126/sciadv.adg0095.

Zhang, P., Nishida, K. & Fang, H., 2025. Reflective body waves extracted from 1 month of global microseisms illuminate the perturbed mantle transition zone beneath SW Japan, *Geophys. Res. Lett.,* **52**(10), e2025GL116419, doi:10.1029/2025GL116419.

Zhang, R., Boué, P., Campillo, M. & Ma, J., 2023. Quantifying *P*-wave secondary microseisms events: a comparison of observed and modelled backprojection, *J. geophys. Int.,* **234**(2), 933–947.